Pore Scale Modeling of Rock Properties and Comparison to Laboratory Measurements

Xin Zhan[1]**,** Lawrence Schwartz[1,2], Wave Smith[2], Nafi Toksöz[1], Dale Morgan[1]

[1] *Earth Resources Laboratory, Massachusetts Institute of Technology, Building 54-1815,*

77 Massachusetts Ave, Cambridge, MA 02139, USA, E-mail: xinzhan@mit.edu

[2] *Schlumberger – Doll Research*

One Hampshire Street, Cambridge, MA, 02139

Abstract

The microstructure of a porous medium and the physical characteristics of the solid and fluid phases determine the macroscopic transport properties of the medium. The purpose of this paper is to test numerical calculations of the geometrical and transport properties (electrical conductivity, permeability, specific surface area, and surface conductivity) of porous, permeable rocks, given their 3D digital microtomography (µCT) images. We focus on µCT data for a 23.6% porosity sample of Berea Sandstone 500 (BS500) with 2.8 micron resolution. Finite difference methods are used to solve the Laplace and Stokes equations for electrical and hydraulic conductivities. We show that the permeability and formation factor are well correlated using a hydraulic radius computed from the digitized image. Electrical transport in the BS500 sample is complicated by the presence of clays. A three phase conductivity model, which includes the double layer length and counter-ion mobility, is developed to compute interface conductivity

from the μCT image and measured values of the cation exchange capacity *(CEC)*. Our calculations compare well with the laboratory measurements on cm^3 core samples. Finally, we examine the influence of image size and image resolution on our numerical results.

Introduction

Understanding the interaction between rock matrix, pore space, and pore fluids at microscopic scale is crucial to better interpretation of macroscopic geophysical measurements. With the development of modern imaging techniques, such as advanced X-ray CT and laser confocal microscopy, direct image of the 3D pore structure of sedimentary rock at micrometer resolution could be obtained. Accurate representation of porous material in digital space makes it possible to compute rock properties according to the physical laws controlling characteristics such as fluid flow and electrical currents (Hazlett, 1995; Coles et al., 1996; Pal et al., 2002). Computational rock physics has become a significant complement to core-derived laboratory measurements and the use of empirical rock physics in the interpretation of logging measurements and resulting reservoir description. Effective characterization of complex rock microstructure at pore scale enables better prediction of physical properties. It reduces the ambiguity of parameters in empirical rock physics models and minimizes the physical and chemical changes of core samples during experimental processes (Klinkenberg, 1941; Amaefule et al., 1986; Li et al., 1995). Advances in computer hardware and computational algorithms make it possible to calculate transport properties on large three dimensional volumes. Increasing the pore space image will reduce the fluctuations of computed properties from small sub-fragments

and minimize the difference between calculated and measured results.

In this study, finite difference (FD) techniques are employed to solve the Laplace equation for electrical conductivity and the Stokes equation for single phase fluid flow (Roberts and Garboczi, 2000). The 3D microstructure is converted into a network of electrical and hydraulic resistors. For the Laplace equation, the boundary conditions (BC) are current and electrical potential normal to the fluid-solid interface are continuous. For the Stokes equation, the boundary condition (BC) is the no-flow condition. In addition to providing the effective value for electrical conductivity and hydraulic permeability, FD techniques could also give the current and flow field distribution at each voxel within the 3D structure. Thus, it is possible to solve multiphysics coupling, such as electrokinetic problems on a microstructure (Pride et al., 1997).

Predicting the formation factor of saturated rocks, particularly with high porosity Fontanbleau sandstones, from a binary image has been successful (Arns et al., 2001, 2005; Pal et al., 2002). The most fundamental empirical relation between brine conductivity and brine saturated rock conductivity is Archie's law (Archie, 1942),

$$F = \frac{\sigma_f}{\sigma_{eff}} = a\phi^{-m}, \tag{1}$$

where F is the formation factor, σ_f and σ_{eff} are fluid and saturated rock conductivities, respectively, Φ is porosity, and m is known as the cementation exponent; depending on lithology, $a \approx 1$ is also a lithological factor. However, this relationship is based on the assumption that the electrolyte conductivity is uniform and the mobile ions are uniformly distributed throughout the pore space. A fluid saturated rock can therefore be modeled as a two-component medium: solid

grains (volume fraction $1-\phi$) and saline water (volume fraction ϕ). This is the basis for calculating the formation factor from digitized binary rock CT microtomography previously (Auzerais et al., 1996; Arns et al., 2001, 2005). This assumption is satisfied by sedimentary rocks such as clay-free sandstones. However, the presence of clay minerals in many rocks puts additional charge carriers in the fluid adjacent to solid surfaces, causing additional conduction along the surface, which is confined to a thin layer known as electric double layer (EDL). The thickness of EDL is defined as the Debye length (Debye and Hückel., 1923; Pride and Morgan, 1991), extending from 30 to 3000 Å from the mineral surface into the neutral electrolyte. Formally, conductivity can be written as the sum of the normal ionic brine conductivity σ_f and a near surface term σ_{surf} due to the double layer. Waxman and Smits (Waxman and Smits, 1968) generalized the electrical behavior of shaly sands into an empirical equation by assuming the surface conduction to be parallel with the bulk conduction for all values of bulk conductivity. The Waxman-Smits model is characterized as the equation

$$\sigma_{\text{eff}} = \frac{1}{F^*}(\sigma_f + BQ_v),$$
(2)

where F^* is the formation factor in the low resistivity limit, Q_v is the cation concentration per unit pore volume (equivalent liter^{-1} or meq ml^{-1}), and B is the average mobility of the counterions close to the grain surface (mho cm^2 meq^{-1}). B is set to increase exponentially with σ_f at a low salinity region and attains a constant maximum at high values of σ_f. This empirical model can capture the nonlinear (convex-upward) behavior of σ_{eff} versus σ_f for shaly sands. More recently, Revil et al. proposed an ionic electrical conductivity model in porous media, with particular emphasis given to surface conduction (Revil and Glover, 1997, 1998; Revil and Leroy,

2001). Their model is based on the description of surface chemical reactions and electrical diffuse layer processes, which gives more depth into the nature of surface conductivity than the empirical Waxman-Smits equation. Revil et al.'s model also contains the parameter Q_v, which signifies the same quantity present in the Waxman-Smits equation. Q_v is related to "Cation Exchange Capacity" *(CEC)* by the equation

$$Qv = \rho_m \big[(1 - \phi)\phi\big] CEC, \tag{3}$$

where ρ_m is grain density (in g cm^{-3}). In shaly sands containing a mixture of clay, the *CEC* is taken as the arithmetic average of the *CEC,* weighted by the corresponding mass fraction of each clay mineral. The surface mobility of the counterions in the EDL is directly introduced in Revil et al.'s model, which is determined by the ionic species present in the saturation brine.

Surface conductivity can contribute substantially to the effective conductivity of the saturated rock, especially in the case of high clay contents and high resistivity brines. In laboratory experiments, the EDL at the fluid-grain surface is naturally present. Therefore, surface conductivity should be included in numerical modeling to compare well with laboratory measurements. Numerical errors should also be considered in order to make an accurate estimation of physical properties from a digital image. The impact of calculation size and image resolution on various properties will be addressed in this paper.

Sample Description and Laboratory Measurements

Our sample is a Berea Sandstone 500 (BS500) core sample with 23.6% porosity. A 3D microtomography image is obtained from the Australia National University (ANU) Digital Core

Lab Consortium. The gray-scale image with brightness corresponding to X-ray attenuation is binarized to clearly distinguish the pore space and rock matrix by ANU. The BS500 core sample is digitized into a 1840^3 voxel tomogram with 2.8 micron resolution. This sample contains some clay; the mineralogy of BS500 is listed in Table 1. The volume fraction of clay was determined by the X-ray attenuation histogram to be 4.03% (very close to mineralogy analysis in Table 1). From an imaging standpoint, a clear binary image separating pore from other mineral phase is expected. However, the low-density inclusions such as clays and feldspars cause spreading in the low density signal, making phase identification more difficult (Knackstedt et al., 2005; Arns et al., 2005). Identification and classification of clay types using petrographic analysis is generally impossible due to the small clay particle size (Minnis, 1984; Knackstedt et al., 2005). The current X-ray μCT imaging technique can recognize clay types in small amounts qualitatively making it possible to determine the volume content for clay minerals (Pike, 1981; Minnis, 1984; Arns, 2005). The ability to determine the spatial relationship of minerals and the size of small particles is still limited by the image resolution and image processing techniques, such as accurate boundary detection in low-density contrast regions. Given limited image resolution, we need to design and interpret our numerical calculations correspondingly.

Micropores under μCT image resolution could exist within clay particles (Asquith, 1990; Wu, 2004). However, the microporosities associated with clays or other fine minerals do not contribute to permeability. Additionally, intragranular macropores and micropores associated with feldspar, sulfate, and carbonates, which are usually either isolated or small, also do not contribute to permeability (Nelson, 2000; Wu, 2004). Thus, as long as the microtomography

captures enough effective porosity, corresponding to the interconnected volume or void space that contributes to fluid flow, we should still be able to give a reasonable prediction on the transport properties.

Laboratory measurements are made on a cylindrical BS500 core sample approximately ~3.7cm and 1 inch in diameter. The formation factor was obtained using an NaCl brine with conductivity 0.2S/m at 25 ^{o}C. Two permeability measurements are carried out, yielding similar results. Gas permeability is measured using Nitrogen (N$_2$); the result, 858 mD, can be converted to liquid permeability using the Klinkenberg correction (Klinkenberg, 1941; Tanikawa and Shimamoto, 2006). Direct liquid permeability is also measured using NaCl brine with 0.2S/m conductivity at 25 ^{o}C by the steady state flow method in the pressure range of 0.05atm to 0.2atm. The BET surface area measurement is based on the volume of Krypton (Kr) gas adsorbed at a sequence of pressure points. Kr provides roughly 300 times greater sensitivity than Nitrogen (N$_2$). All the laboratory measurement results are listed in Table 4.

Numerical Calculations

Electrical Conductivity Calculation

The effective DC conductivity of a random material can be solved by Ohm's Law. The conductivity value σ of a composite n-phase material is a function of location r. For steady state conductivity problems, where the currents are steady in time, the charge conservation equation possesses the same form as the Laplace equation. Between phases having different conductivities,

the boundary conditions require that the current density normal to the interface and the potential are continuous. We can calculate the macroscopic conductivity of the random material by applying an electric potential gradient across the sample. The volume averaged current density can be used to compute the effective conductivity from Ohms' law.

We use a stagger-grid finite difference scheme with 2nd order accuracy in space. The grid interval in the x-, y- and z- direction is exactly the same as the CT image resolution, 2.8μm. As for the material properties, our modified finite difference electrical conductivity programs can handle arbitrary diagonal conductivity tensors. The intrinsic challenge of solving the Laplace equation of high contrast conductivity value for neighboring grids is overcome by adopting a gradual relaxation method. For formation factor estimation, we could ideally assign $\sigma_{mineral} = 0$ and to the pore fluid $\sigma_f = 1$. The normalized fluid filled rock conductivity σ_{eff} gives the formation factor. We can also define the solid matrix to be quartz conductivity, and saturation fluid can have a conductivity contrast of 1-15 orders in magnitude. This could provide us with an absolute value for the fluid filled rock conductivity.

Permeability Calculation

Permeability is a measure of the resistance to fluid flow under a pressure gradient of a given porous medium. The mechanism of fluid flow is given by the Navier-Stokes equation. For the case of laminar (slow, incompressible) flow, the fluid flow can be conveniently described by the linear Stokes equations:

$$\eta \nabla^2 \vec{u}(\vec{r}) = \nabla P(\vec{r}), \tag{4}$$

$$\nabla \cdot \vec{u}(\vec{r}) = 0 \quad , \tag{5}$$

where u and P are the local velocity vector and pressure fields at position $\vec{r}$, and η is the dynamic viscosity of the fluid. We can calculate the macroscopic permeability of the porous medium by applying a potential gradient across the sample. The permeability, κ, of the porous medium is calculated by volume averaging the local fluid velocity (in the direction of the flow) and applying the Darcy equation:

$$u = -\frac{\kappa}{\eta}\frac{\Delta P}{L} \tag{6}$$

where u is the average fluid velocity in the direction of the flow for the porous media and L is the length of the sample porous medium across which there is an applied pressure gradient of ΔP.

To solve the hydraulic problem, we use a modified Stokes solver based on an industry standard finite difference (FD) code developed at NIST (National Institute of Standards and Technology, Gaithersburg, MD 20899-8621, U.S.A) (Schwartz et al., 1993; Nicos et al., 1994; Bentz and Martys, 2007). We also test the applicability of the conductivity-permeability relationship on the same structure by solving two different PDEs using a uniform FD scheme. The correlation between numerically computed electrical conductivity and permeability will be examined using Paterson's model (Paterson, 1983).

Surface Area Calculation

We perform all the numerical calculations on the 3D CT microtomography, which is a binary image. This binary image has been quantized to two values, _0_ denoting the pore space and

1 denoting the solid matrix after segmentation and thresholding the original grey level X-ray tomography. To quantify the surface area from the binary image, we need to identify pixels at the pore-grain interface. Two different image processing methods are adopted. The first method is a gradient method, specifically, first order differential methods of edge detection (Canny, 1986; Pathegama et al., 2004). An odd symmetric filter $\begin{bmatrix} -1 & 0 & -1 \\ -1 & 0 & -1 \\ -1 & 0 & -1 \end{bmatrix}$ will approximate a first derivative, and peaks in the convolution output will correspond to edges (surface pixel) in the image. The second method is based on tracing phase connectivity to identify a phase change. Binary image is classified into two opposite classes: inner pixel and surface (edge) pixel. Checking the connectivity of the *0* phase to the *0* phase in its 8 neighbors in 3D, the zero-connectivity pixels are inner points or isolated points. Eliminating those inner and isolated points from the original image gives the surface (edge) pixel (Zahn, 1971). Given the continuous nature of the binary image for rock CT microtomography, these two algorithms should be able to mark as many real surface pixels as possible. The surface area is usually expressed as square meters of surface per gram of solid. By multiplying by the grain density (2.65g/cm^3), we can transfer the numerically solved surface area from square meters per cube meters of solid to per gram of solid as expressed in the laboratory measurements. Both methods give similar results and we take their average as our count of the surface pixels. We take the mean value of surface area computed from two different methods, which is listed in Table 3 and 4.

Discussions

Comparison of Numerical Computation to Laboratory Measurements

Five 400^3 sub-volumes at different locations are selected in the total 1840^3 volume as shown in Figure 1. We use porosity as the criteria to pick representative sub-sets within the whole volume and avoid picking the edges. Sub-volume 3 is in the middle of the total volume. Sub-volumes 1, 2, 4, and 5 are located, respectively, northwest, northeast, southwest and southeast of sub-volume 3 to capture both vertical and horizontal heterogeneity. The hydraulic and electrical flux for one slice in sub-volume 3 are color mapped (on a logarithmic scale) in Figure 2. For display purposes, we chose a 200^3 sub-volume in the middle of 3 (Fig 2.a); the most complex pore geometry was found to be in the X-Y plane (Fig 2.b). The electrical flux shows higher amplitude than the hydraulic flux in the thin and narrow pores (Fig 2.c and 2.d). The identified surface pixels are shown in red along the pore (blue) – grain (green) boundary in Figure 3.

We could compute the effective conductivity of the BS500 sample with a different saturation phase, such as gas, oil, and brines with different salinities based on our modified Laplace solver. For the saturation phase, we use the realistic conductivity value for a different fluid instead of *1* as a normalized conductivity, which is the case in previous studies. The grains could be given the quartz conductivity of $10^{-14} S/m$ instead of *0*. To compute the formation factor, we could use either *0* versus *1* or more physically, use a highly conductive brine,

$10^{-1} S/m$ versus $10^{-14} S/m$ system. The saturated rock conductivities, σ_{eff}, with different

saturation phases are listed in Table 2. Similar to Figure 2.c, Figure 4.a and 4.b correspond to the

electrical flux with oil and gas saturation, respectively. With an increase of the conductivity

contrast between the saturation phase and host grain phase, the boundary between the pore space

and grain becomes sharper. These sharper contrasts can better resolve the details of the structure.

Porosity, formation factor, permeability, and surface area of the five sub-volumes computed

from the 3D tomography are listed in Table 3. The variation in porosity is within 5% for five

400^3 sub-fragments, which indicates our calculation size is representative. Heterogeneity of the

geometry at different locations of the core sample is reflected in both formation factor and

permeability. An isolated or extensive inclusion, small in volume, could block the flow without

much impact on the porosity (Kameda, 2004). Thus, conducting computations on a large volume

is always preferred. Here, we also calculate the mean value and variance for these five sets of

data and compare with the laboratory measurements in Table 4. The numerical computations on

the mm^3 images compares well with the laboratory measurements on the cm^3 core sample by

taking the mean value of different sub-volumes.

Formation Factor and Permeability Correlation

Correlating hydraulic permeability to other physical properties of the porous media

continues to be an issue. The most popular technique is to relate permeability with electrical

conductivity through pore volume to surface area (V_p/S), based on the assumption that

electrical and fluid stream lines are identical. Meanwhile, electrical conductivity is usually easier

to measure in the laboratory or in situ than permeability. We have numerically calculated electrical conductivity, permeability, and surface area on the same structure. We want to test whether we can establish the correlation among those computed physical properties from the CT image.

A consistent development of the equivalent channel for both fluid flow and electrical conduction in porous media leads to the expression:

$$\kappa = \frac{CR^2}{F} \quad , \tag{7}$$

where k is permeability, F is the formation factor, C is a geometrical factor, and R is the so called hydraulic radius (Brace, 1977; Paterson, 1983; Walsh and Brace, 1984). C is in the range of $\frac{1}{2}$ for circular pores to $\frac{1}{3}$ for a slot, which cover the widest range of aspect ratio of most porous media (Wyllie and Gregory, 1955). The concept of hydraulic radius was first developed for pipes of non-circular section, where it is defined by the ratio of the perimeter to the cross-sectional area under the assumption of uniformity along the length. In porous media, hydraulic radius R can be determined by the ratio of porosity and surface area (ϕ/S). Thus, R represents an equivalent (or average) hydraulic radius of the exceedingly complicated flow channels. From this empirical relationship, we could see that permeability is inversely proportional to the formation factor.

The computed physical properties for five 400^3 sub-volumes described above are given in Table 4. We cross plot the computed permeability and formation factor of five sub-cubes as shown in Figure 5. An inverse linear trend could be observed between F and k due to the small fluctuation of porosity and surface area in five cubes. There are three ways to calculate the

hydraulic radius R. Taking the calculated F and permeability k in Table 3 into Eq. (7), with shape factor C preferably chosen to be 0.4 (Paterson, 1983), we could back out the hydraulic radius to be 3.38μm. The other two methods are based on the definition of hydraulic radius. We can simply take the ratio of porosity and surface area from laboratory measurement and numerical computation (Table 4), respectively. The laboratory determined R is 2.39 μm, numerically computed R is 2.97 μm. Gratifying agreement among three numbers is obtained. Correlating different physical properties that are numerically solved independently allows us to deduce one property from others. The characteristic pore size, which is twice the hydraulic radius, is larger than the image resolution. A good permeability prediction could be expected with this high image resolution.

Surface Conductivity Calculation and Laboratory Measurements

Another long standing question is how to best model the surface conductivity associated with clay in shaly sand (Waxman and Smit, 1968; Clavier et al., 1977; Johnson et al., 1986; Sen and Kan, 1987; Lima and Sharma, 1990; Revil et al., 1998; Devarajan, 2006). The authigenic clays, the most common type of clay, can be divided into three morphologic groups (Neasham, 1977). Pore lining, pore bridging, and discrete particle correspond to illite and smectite, chlorite, and kaolinite, respectively. The "cation exchange capacity" (*CEC*), which indicates the maximum number of surface exchangeable cations per unit mass of shaly rock, also strongly depends on clay mineral type (Patchett, 1975). Given the complexity of morphology, particle size, and chemical properties of clay minerals, treating the surface conductivity of clays as an

electrically equivalent effective conductivity is always a preferable method. To derive the surface conductivity from CT images of microstructure, especially with the limit of accurate identification and location of individual clay minerals, the same approach needs to be adopted. The clay aggregate with its bounding water – either coating over or dispersed among the sand grains – is treated as a highly compacted layer with asymptotic conductivity (Johnson et al., 1986; Lima and Sharma, 1990). Also, from the mineralogy report (provided by Schlumberger-Doll Research), illite and kaolinite are the two major types of clay existing in our BS500 core sample. Thus, the effective conductivity model should be applicable for our specific sample.

In contrast with previous work, our aim is to numerically compute surface conductivity on the 3D microtomography of a Berea Sandstone core sample. First, in most of previous studies, solid grains are modeled as spheres to a first order approximation for simplicity (Johnson et al., 1986; Lima and Sharma, 1990; Devarajan, 2006; Toumelin, 2008). Second, in the previous semi-analytic equations or numerical models, some parameters are adjusted to fit certain datasets or to simulate certain empirical relationships. Our three-phase conductivity model is built on the microtomography of porous rock, which is more complex in structure than sphere packs. Also, we have direct laboratory measurements on the *CEC* value from the core sample to account for the contribution from each clay mineral. We can also calculate the *CEC* value from the clay volume fraction, determined by X-ray attenuation histogram. Pore scale computation is carried out on 2.8 micron resolution grids. Thickness of the clay bound water layer (EDL) in different salinity electrolytes is directly taken from the definition and calculation of Debye length. Pore fluid is divided into free water and bound water. Bound water exists along the grain-electrolyte

boundary (surface voxel). Effective porosity (pore space voxels) is maintained without any structural change. We first validate our three-phase model on synthetic porous medium composed of spheres on uniform radius – Finney pack (Finney, 1970) with the analytic expression:

$$\sigma_{\text{eff}} = \frac{1}{F}(\sigma_f + \frac{2\Sigma_{surf}}{\Lambda}) \equiv \frac{\sigma_f}{F}(1 + X),\tag{8}$$

where Σ_{surf} indicates surface conductance, Λ is a weighted surface to volume ratio, and X is a simple additive term in the range of 1-10 depending on rock type (Devarajan, 2006). For a given X, we can calculate Σ_{surf} as $\frac{\Lambda X}{2}$ with the surface to volume ratio obtained from Finney pack microstructure. Putting Σ_{surf} into the three–phase model, which will be described in detail below, we can numerically obtain the same effective conductivity value as in the Waxman-Smits formula by solving the Laplace equation.

Using a two–phase model (pore fluid and grain) will underestimate the saturated rock conductivity, σ_{eff}, with the presence of clays. Thus, we change our model from two-phase to three-phase to include the surface conductivity at grain-electrolyte boundary. All the surface pixels (as described above) contain an EDL. The thickness of the EDL (χ_d) is at the nanometer scale and image resolution is at micrometer scale. Surface pixels at the pore-grain boundary are defined to be the third phase. Numerical representation of the porous rock is changed to a three–phase model as illustrated in Figure 6. In the three–phase conductivity model, the first kind of grid cell has the conductivity of σ_1, equal to the rock matrix conductivity. The second kind of grid cell has the conductivity of σ_2, equal to the free electrolyte conductivity in the pore space.

The third kind of grid cell is the boundary grid containing an EDL at the fluid-solid interface with the conductivity σ_3. The conductivity model in the third kind of grid is illustrated in Figure 7. We calculate σ_3 by geometrically averaging the larger surface conductivity, σ_{surf}, over the double layer thickness, χ_d, with σ_2 in the remainder of the boundary grid ($L - \chi_d$). This geometric average is physically feasible since surface conductivity in the EDL and the free electrolyte in the pore space could be treated as two conductors in parallel.

To quantify σ_3, we need to determine the surface conductivity, σ_{surf}, in the EDL. The surface of grains which composes the solid matrix of sandstones is typically charged when in contact with an electrolyte. The counterions required to balance the mineral surface charge form the EDL (Revil and Glover, 1998). Surface conductivity depends on both physical and chemical properties of the electrolyte and the microstructure, as defined by Kan and Sen (Kan and Sen, 1987),

$$\sigma_{surf} = \frac{2}{3}\left[\frac{\phi}{1-\phi}\right]\beta_S Q_v \Lambda^{-1}, \quad Qv = \rho_m\left[(1-\phi)\phi\right]CEC. \tag{9}$$

Here, ρ_m is grain density (in g cm^{-3}), β_s is the surface mobility of the counterions, Λ is the weighted pore surface to volume ratio, and Q_v has the same meaning as in Waxman-Smits equation (Waxman and Smits, 1968), which is related to "Cation Exchange Capacity" (*CEC*). For sodium chloride electrolyte, the counterions in the electrolyte are N_a^+ with surface mobility of $\beta_s = 5.14 \times 10^{-9}$ m^2 s^{-1} V^{-1} at 25°C (Waxman and Smits, 1968; Patchett, 1975). Q_v could be obtained from *CEC* if available or it could be computed from clay content, V_{sh}, and porosity using

$$Qv = V_{sh}/(1-\phi) \times 1.5 . \tag{10}$$

We have both measured the *CEC* value [*0.27 meg/100g*] and the clay content from the X-ray

attenuation histogram. Thus, we can calculate surface conductivity, σ_{surf}.

The last parameter to be determined for σ_3 calculation is the EDL thickness, which is the so

called Debye length, χ_d. Debye length is defined as (Debye and Hückel., 1923; Pride and

Morgan, 1991; Zhan, 2005)

$$\chi_d = \sqrt{\varepsilon_f k_B T / e^2 z^2 N} \tag{11}$$

,where ε_f is the fluid permittivity, k_B is the Boltzman constant, T is absolute temperature,

e is the electric charge, z is the ionic valence of the solution, and N is ion concentration,

defined as $N = 6.022 \times 10^{26} \times molarity$. Some typical values of the Debye length as a function of

ionic strength $I = \frac{1}{2} \times z \times N$ are given in Table 5(Morgan et al., 1989).

Thus, the surface voxel conductivity, σ_3, could be calculated as a function of electrolyte

conductivity, σ_2. By solving the Laplace equation with three different conductivity components

at different locations within the 3D microstructure, we can predict the conductivity of the BS500

core sample, σ_{eff}, in a wide range of salinity environments.

Laboratory measurements are carried out to measure the electrical conductivity, σ_{eff}, on

the saturated BS500 core sample. To avoid the chemical changes in the sample, such as clay

swelling and liberation after the saturation, especially with highly resistive electrolyte saturation,

we use freshly cut samples. Samples are cut into cylinders of approximately ~2cm length by

~1inch diameter from the same BS500 block. Ten samples are saturated in NaCl brines of

conductivity 0.001*S/m*, 0.003*S/m*, 0.01*S/m*, 0.025*S/m*, 0.05*S/m*, 0.2*S/m*, 0.4*S/m*, 1*S/m* and 2*S/m*,

respectively. The brine is prepared by adding different amounts of sodium chloride into deionized water. Each sample is vacuum-impregnated with brine in order to expel air and then fully saturated. Saturated samples are never allowed to dry out during the conductivity measurements. Non-polarized Ag/AgCl electrode disks are attached to both sides of the sample for resistivity measurements. Laboratory measurements and numerical calculations are shown in Figure 8. In the high salinity region, the two-phase model works well to predict the linear relationship between the saturated rock conductivity, σ_{eff}, and the electrolyte conductivity, σ_f, (dashed line in Figure 8). The ratio between this two is the formation factor. When the electrolyte conductivity is low and the surface conductivity cannot be neglected, the three-phase model is needed to capture the convex-upward trend (solid line in Figure 8).

Numerical Error Analysis

Two sources of numerical error are considered: the resolution of the image and the size of computation volume. Using finite size voxel limits our ability to resolve the smallest features of the pore space. To test the importance of this effect we generate a sequence of models with successively poorer resolution by doubling the voxel edge length. Eight high resolution voxels form one low resolution voxel with a simple majority rule were used to assign the new voxel to be either pore or grain. The five models then vary from the original 400^3 with 2.8 μm resolution to 25^3 with 44.8 μm resolution. Four downscaled cubes from the 400^3 cubes (sub-set #3 in Figure 1.a) are shown in Figure 9. The connectivity of pore space is largely reduced with decreasing resolution.

Porosity, permeability, formation factor, and surface area were calculated for the five models. The fractional changes in these quantities relative to the original 400^3 with 2.8 μm resolution are plotted in Figure10. The electrical conductivity is most affected by this process. This is expected since using coarser grids to resolve a structure tends to describe the curved grain boundaries inaccurately and close narrow pores. Closure of the narrow pores will impact the electrical current more severely than hydraulic current (as discussed in Figures 2.c and 2.d). By conducting this image resolution analysis, we can quantify the discretization error at each resolution level. This is especially important if we want to use coarser grids to resolve physically larger volumes at a given level of computational power.

Finally, we consider the effect of enlarging our model from 400^3 to 800^3, both with 2.8 μm resolution. We optimize the Laplace solver to allow dynamic allocation of memory. Computaion demands are heavy: a single conductivity run at 800^3 cube scale would require ~10 Gbytes of memory and 15 CPU hours to complete on a Intel Quad-Core Xeon 3GHz processor. In the 800^3 model, we get ***13.75*** for electrical formation factor, which is much closer to the experimental value than taking the average of five 400^3 sub-volumes. Thus, the choice of representative computation cell size is important. Within the capacity of computational power, large sampling volume is always preferable.

Conclusions

In this paper, we present different physical properties of a Berea Sandstone sample with 23.6% porosity computed using μCT microtomography. The following conclusions are made:

1. A uniform finite difference (FD) scheme is applied to solve the Laplace equation for the electrical problem and the Stokes equation for the Hydraulic problem. The Laplace solver is modified to handle different levels of conductivity contrast. Electrical conductivity of the BS500 core sample saturated with gas, oil, and brines are computed. Two different image processing methods are applied to recognize surface voxel in the digital binary image. Five 400^3 sub-volumes at different locations within the core sample are choosen to compute porosity, permeability, electrical conductivity, and specific surface area. All five sub-volumes possess similar porosities, which are close to laboratory measurements. We also computationally establish the correlation linking permeability to electrical conductivity through geometric properties, such as hydraulic radius, which can also be calculated from the 3D microtomography. Numerically and experimentally determined hydraulic radius are consistent. Numerically computed porosity, permeability, electrical conductivity, and surface area compare well with the laboratory data taken on cm-scale core samples.

2. A three phase model is developed to compute surface conductivity. The *CEC* value for the BS500 core sample is obtained both experimentally and computed from clay content. The length of electrical double layer (EDL) is determined by definition and varies with electrolyte salinity. Counterion mobility is taken to be the value of the ionic species present in the experiment. Laboratory measurements are designed to measure the electrical conductivity of the BS500 core sample saturated with NaCl brine in different salinity ranges (fluid conductivity from 0.001*S/m* to 2*S/m*). Two-phase model works well when the brine conductivity is high, giving an accurate prediction of the formation factor. Surface conductivity needs to be taken into account using

three-phase model in the low salinity regimes.

3. The effects of image resolution on computed physical properties are investigated using majority rule. Decreased resolution leads to decreased permeability and electrical conductivity. Optimization of computation algorithm enables us to perform calculations on large 3D volume.

Acknowledgements

References

Amaefule, J.O., Wolfe, K., Walls, J.D., Ajufo, A.O. and Paterson, E.: 1986, Laboratory determination of effective liquid permeability in low-quality reservoir rocks by the pulse decay technique, *paper SPE 15149 presented at the 56th California Regional Meeting, Soc. Of Pet. Eng.,Oakland,Calif,* April 2-4.

Archie, G.E.: 1942, The electrical resistivity log as an aid in determining some reservoir characteristics, *Trans. AIME*, **146**, 54-62.

Arns, C. H.: 2001, The influences of morphology on physical properties of reservoir rock, *Ph.D. thesis, Univ. of New South Wales*.

Arns, C.H., Bauget, F., Ghous, A., Sakellariou, A., Senden, T.J., Sheppard, A.P., Sok, R.M., Pinczewski,W.V., Kelly, J.C. and Knackstedt, M.A.: 2005, Digital core Laboratory: Petrophysical analysis from 3D imaging of reservoir core fragments, *Petrophysics*, **46**, 260-277.

Asquith, G.B.: 1990, Log evaluation of shaly sandstones: a practical guide, *AAPG continuing education course note series #31*, 59P.

Auzerais, F.M., Dunsmuir, J., Ferréol, B.B., Martys, N., Olson, J., Ramakrishnan, T.S., Rothman, D.H. and Schwartz, L.M.: 1996, Transport in sandstones: A study based on three dimensional microtomography, *Geophysical Research Letters*, **23**, 705-708.

Bentz, D.P. and Martys, N.S.: 2007, A stokes permeability solver for three-dimensional porous media, *NISTIR 7416, U.S. Department of Commerce*.

Brace, W.F.: 1977, Permeability from resistivity and pore shape, *J.Geophys.Res*, **82**, 3343-3349.

Canny, J.: 1986, A computational approach to edge detection, *IEEE Trans. Pattern Analysis and Machine Intelligence*, **8**, 679-714.

Coles, M. E., Hazlett, R.D., Muegge, E.L., Jones, K.W., Andrews, B., Siddons, P., Peskin, A. and Soll, W.E.: 1996, Developments in synchrotron X-Ray microtomography with applications to flow in porous media, paper SPE 36531, *Proc. 1996 SPE Annual Technical Conference and Exhibition, Denver*, Oct 6-9.

Debye, P. and Hückel, E.: 1923, Zur theorie der electrolyte, *Phys. Z*, **24,** 185-206.

Devarajan, S., Toumelin, E. and Torres-Verdín, C.: 2006, *SPWLA 47th Annual Logging Symposium*, June 4-7.

Finney, J.: 1970, Random packings and the structure of the liquid state, *Proc. Roy. Soc,* **319A**,

479.

Garbozi, E.J.: 1998, Finite Element and Finite Difference Programs for Computing the Linear Electric and Elastic Properties of Digital Image of Random Materials, *NISTIR* **6269**.

Hazlett, R.D.: 1995, Simulation of capillary dominated displacements in microtomographic images of reservoir rocks, *Transport in Porous Media*, **20,** 21-35.

Johnson, D.L., Koplik, J. and Schwartz, L.M.: 1986, New pore-size parameter characterization transport in pours media, *Physical Review Letters*, 57, **n.20**, 2564-2567.

Kameda, A.: 2004, Permeability evolution in sandstone: digital rock approach, *Ph.D. thesis, Stanford University.*

Kan, R. and Sen, P.N.: 1987, Electrolytic conduction in periodic arrays of insulators with charges, *J. Chem. Phys*, **86,** 5748-5756.

Klinkenberg, L.J.: 1941, The permeability of porous media to liquids and gases, *Drill. Prod. Pract,* **8**, 200-213.

Knackstedt, M.A., Arns, C.H., Limaye, A., Sakellariou, A., Senden, T.J., Sheppard, A.P., Sok, R.M., Pinczewski, W.V. and Bunn, G.F.: 2004, Digital Core Laboratory: Properties of reservoir core derived from 3D images, SPE-87009; *presented at the 2004 Asia Pacific Conference on Integrated Modelling for Asset Management, Kuala Lumpur*.

Li, S.X., Pengra, D.B. and Wong, P. Z.: 1995, Onsager's reciprocal relation and the hydraulic permeability of porous media, *Phys. Rev. E,* **59,** 2049-2059.

Lima, O.A.L. and Sharma, M.M.: 1990, A grain conductivity approach to shaly sandstones, *Geophysics*, **55**, n.10, 1347-1356.

Morgan, F.D., Williams, E.R. and Madden, T.R.: 1989, Streaming potential properties of westerly granite with applications, *Journal of Geophysical Research,* **94,** 12449-12461.

Minnis, M.M.: 1984, An automatic point-counting method for mineralogical assessment, *The American Association of Petroleum Geologists Bulletin*, **68,** P744-752.

Neasham, J.W.: 1977, The morphology of dispersed clay in sandstone reservoirs and its effect on sandstone shaliness, pore space and fluid flow properties, *SPE paper,* **6858**.

Nelson, P.H.: 2000, Evolution of permeability-porosity trends in sandstones: *Society of Professional Well Log Analysts 41st Annual Logging Symposium*, June 4-7.

Nicos, S., Martys, N.S., Torquato, S. and Bentz, D.P.: 1994, Universal scaling of fluid permeability for sphere packings, *Phys. Rev. E*, **50**, 403-408.

Pal, E.R., Stig, B.: 2002, Process based reconstruction of sandstones and prediction of transport properties, *Transport in Porous Media***, 46,** 311-343.

Patchett, J.G.: 1975, An investigation of shale conductivity, *SPWLA***,** *16th Annual Logging Symposium***,** Paper **U,** 40pp.

Paterson, M.S.: 1983, The Equivalent Channel Model for Permeability and Resistivity in Fluid Saturated Rock-a Re-appraisal, *Mechanics of Materials*, **2**, 345-351.

Pathegama, M. and Göl, Ö.: 2004, Edge-based image segmentation, *Proceedings of the International Conference on Computational Intelligence,* ISBN **975-98458-0-6**.

Pike, J.D.: 1981, Feldspar diagenesis in Yowlumne sandstone, Kem County, California: *M.S. thesis, Texas A&M University, College Station, TX*

Pride, S. R. and Morgan, R. D.: 1991, Electrokinetic dissipation induced by seismic waves,

Geophysics, **56**, 914-925.

Revil, A. and Glover P. W. J.: 1997, Theory of ionic-surface electrical conduction in porous media, *Phys. Rev. B,* **55,** 1757-1773.

Revil, A. and Glover P. W. J.: 1998, Nature of surface electrical conductivity in natural sands, sandstone, and clays, *Geophysical Research Letters,* **25,** 691-694.

Revil, A., Cathles III, L.M., Losh, S. and Nunn, J.A.: 1998, Electrical conductivity in shaly sands with geophysical applications, *Journal of Geophysical Research*, **103**, n. B10, 23925-23936.

Revil, A. and Leroy, P.: 2001, Hydroelectric coupling in a clayey material, *Geophysical Research Letters,* **28,** 1643-1646.

Schwartz, L.M., Martys, N.S, Bentz, D.P., Garboczi, E.J. and Torquato, S.: 1993, Cross-property relations and permeability estimation in model porous media, *Phys. Rev. E,* **48,** 4584-4591.

Sen, P.N. and Kan, R.: 1987, Electrolytic conduction in porous media with charges, *Phys. Rev. Lett*, **58**, 778-780.

Tanikawa, W. and Shimamoto, T.: 2006, Kinkenberg effect for gas permeability and its comparison to water permeability for porous sedimentary rocks, *Hydrology and Earth System Sciences Discussions*, **3**, 1315-1338.

Wu, T.: 2004, Permeability prediction and drainage capillary pressure simulation in sandstone reservoirs, *Ph.D. thesis, Texas A&M University*.

Toumelin, E. and Torres-Verdín, C.: 2008, Objected-oriented approach for the pore-scale simulation of DC electrical conductivity of two-phase saturated porous media, *Geophysics*, **73**, E67-E79.

Walsh, J. B. and Brace, W. F.: 1984, The effect of pressure on porosity and transport properties of rock, *J.Geophy. Res,* **89**, 9425-9431.

Waxman, M.H and Smits, L.J.M.: 1968, Electrical conduction in oil-bearing sands, *Society of Petroleum Engineers Journal*, **8**, 107-122.

Wyllie, M.R.J. and Gregory, A.R.: 1955, Fluid flow through unconsolidated porous aggregates. Effect of porosity and particle shape on Kozeny-Carman constants, *Ind. Eng. Chem*, **47**, 1379.

Zahn C.: 1971, Graph-Theoretic Methods for Detecting and Describing Gestalt Clusters, *IEEE Trans. Computers*, **20**, 68–86.

Zhan, X.: 2005, A study of seismoelectric signals in measurement while drilling, *M.S. thesis, Massachusetts Institute of Technology*.

Composition	Volume Fraction (%)
Quartz	88.9
Clay	3.9
Feldspar	3.4
Carbonate	2.2
Evaporite	0.5
Others	1.1

Table 1: Mineralogy of Berea Sandstone 500 core sample (provided by Schlumberger Doll Research)

(a)

(b)
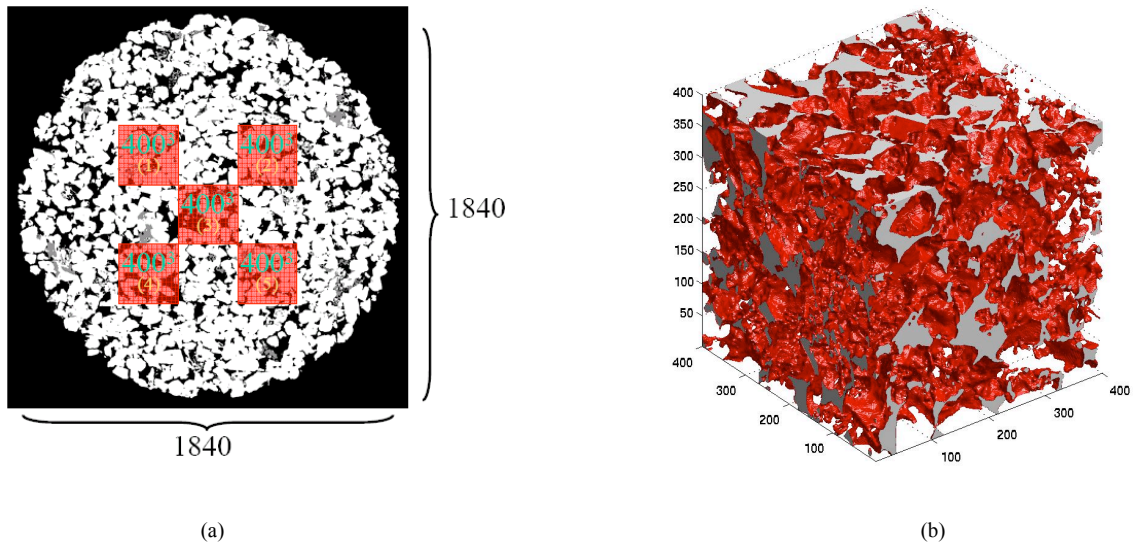
Figure 1: (a) Z direction view of selected five 400^3 sub-volumes at different locations in the total 1840^3 BS500 core sample with 2.8 micron resolution. X-ray intensity values are encoded in gray shades. Brightness corresponds to increased intensity. #3 sub-volume is in the middle of the total volume. (b) The pore cast (shown in red) of #3 sub-volume.
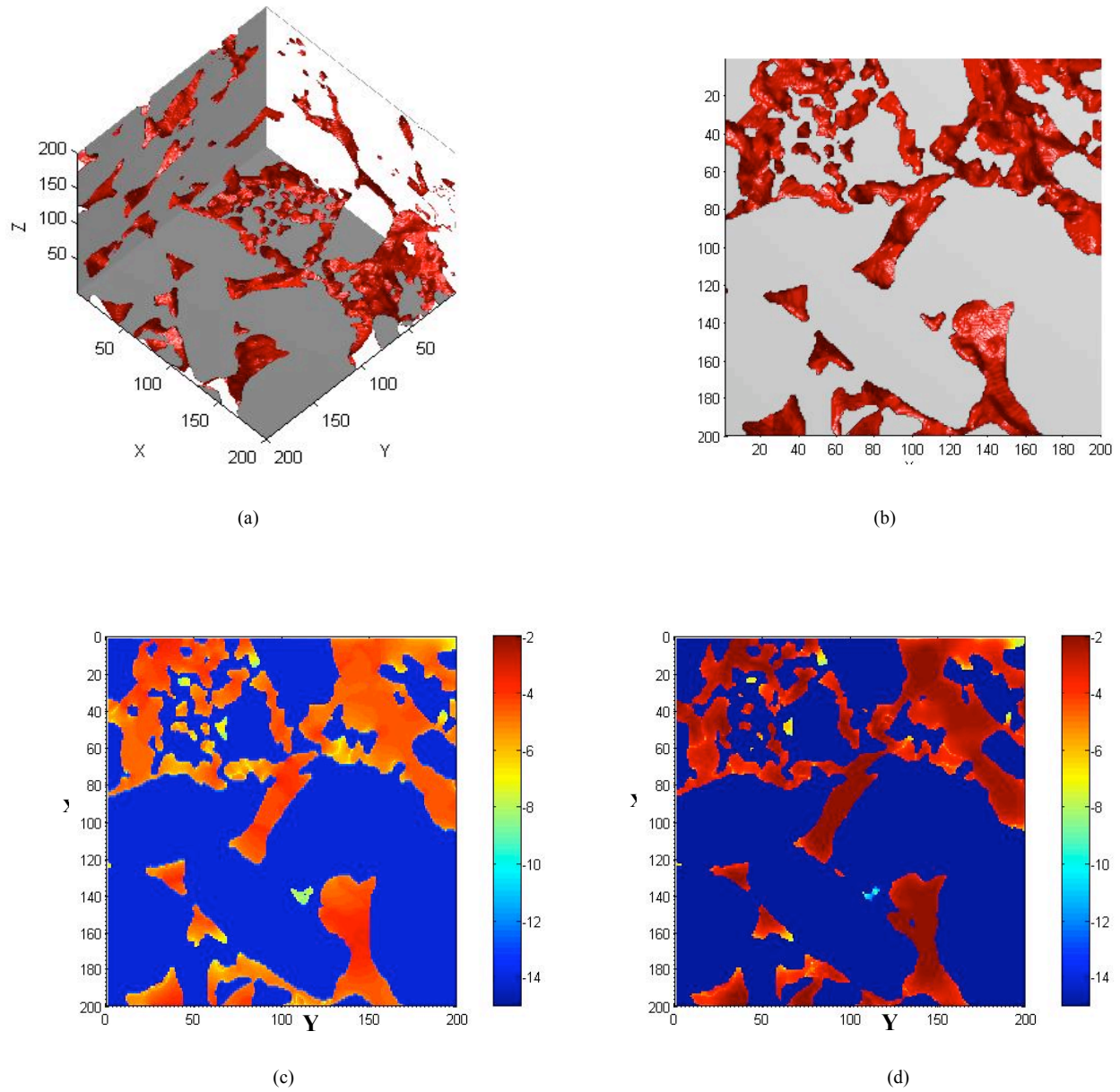
Figure 2: (a) 3D tilted view of a 200^3 cube in #3 sub-volume in Fig 1.b (red indicates pore space, grey indicates grain) (b) X-Y plane of the first slice in Fig 2.a. (c) Electrical flux of Fig 2.b in logarithm scale. (d) Hydraulic flux of Fig 2.b in logarithm scale.
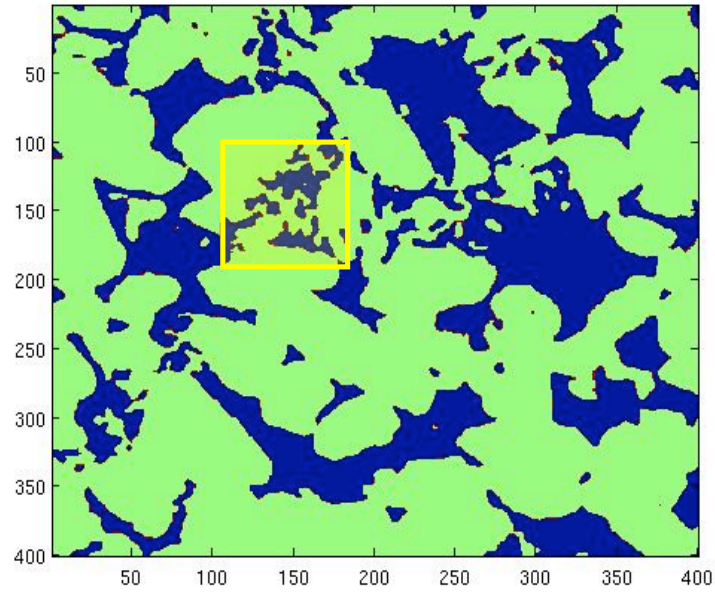
(a)
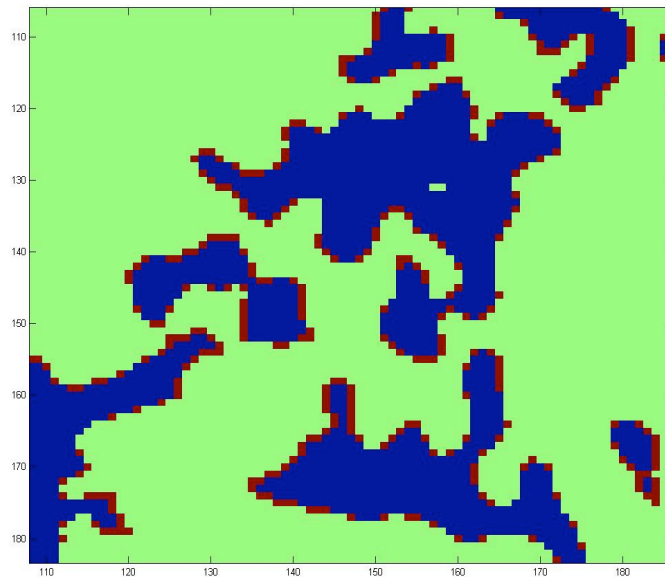
(b)

Figure 3: (a) Surface pixel (red) along pore (blue) – grain (green) boundary using gradient based image processing method. This is one slice in sub-volume #3. (b) Enlarged view of shadowed area (yellow square) in Fig 3.a. Surface pixels are shown in red, pore in blue and grain in green.

Saturation Phase	Gas	Oil	Saline Water			
Saturation Fluid Conductivity (S/m)	$1e^{-11}$	$5e^{-9}$	$1e^{-1}$	1	10	10
Effect Conductivity (S/m)	$6.16e^{-13}$	$3.01e^{-10}$	Archie's Law			

Table 2: The effective conductivity of BS500 saturated with gas, oil and saline water. For highly conductive brine in the table, saturated rock conductivity and electrolyte conductivity obeys Archie's law. The ratio between electrolyte conductivity and saturated rock conductivity is a constant, formation factor, and provided Table 3 below.

(a)

79

(b)
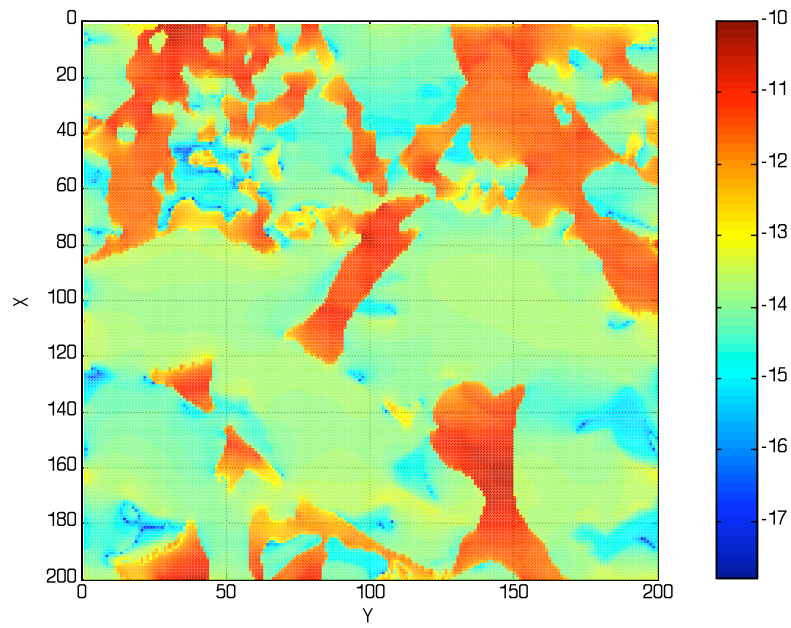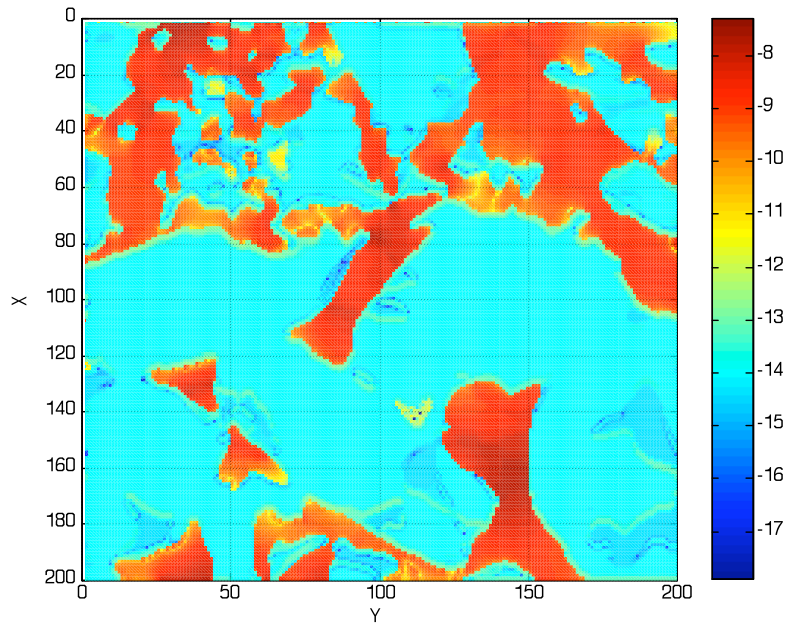
Figure 4: (a) Electrical flux of Fig 2b saturated with gas in logarithm scale. (b) Electrical flux of Fig 2b saturated with oil in logarithm scale.

	#1	#2	#3	#4	#5
Porosity (%)	22.98	23.33	23.81	24.10	23.60
Formation Factor	22.23	18.69	16.11	11.98	16.31
Permeability (Darcy)	0.38	0.61	0.75	1.05	0.83
Surface Area (m^2/g)	0.88	0.81	0.78	0.69	0.77

Table 3: Numerically computed porosity, permeability, formation factor and surface area of the five selected sub-volumes in Fig 1a.

	Laboratory		Numerical
Porosity (%)	23.56		*23.64* $\pm$ 0.43
Formation Factor	13.03		*16.40* $\pm$ 3.76
Permeability (Darcy)	Gas	Liquid	*0.60* $\pm$ 0.23
	0.89	0.45	
Surface Area (m^2/g)	0.93		*0.77* $\pm$ 0.02

Table 4: Mean value (bold italicized number in column 3) and variance (second number in column 3) of different parameters for five sub-volumes are compared to laboratory measurements.
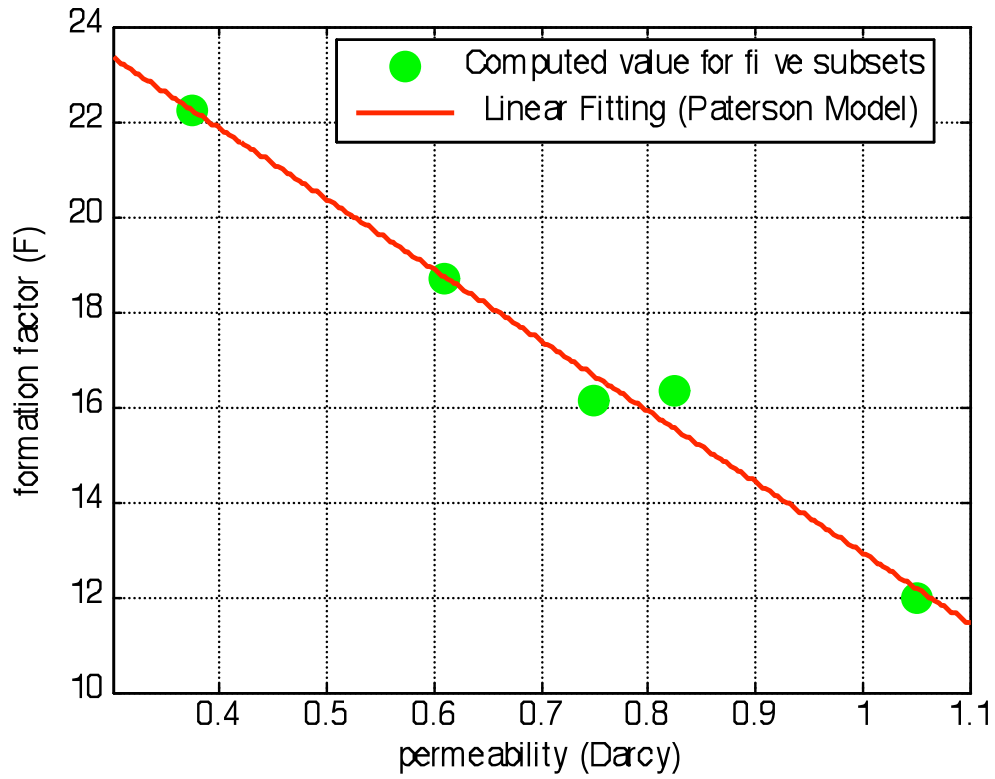
Figure 5: Numerically calculated permeability v.s numerically calculated formation factor (green dots) for 5 400^3 sub-volumes (Fig 1a) in Berea Sandstone 500. Linear relationship between formation factor and permeability indicated by Paterson Model (Paterson, 1983).
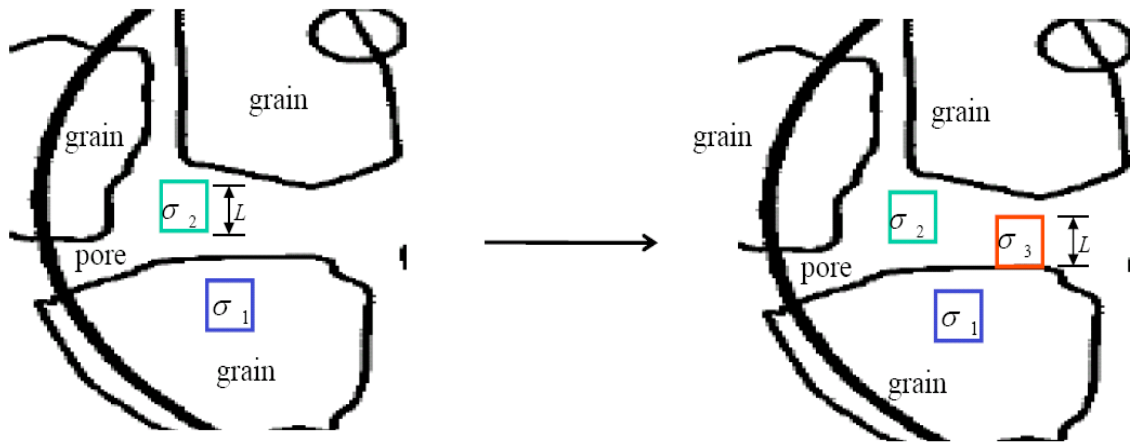
Figure 6: Two-phase representation of the porous rock (left) and three-phase representation of the porous rock (right). Both models have the same grid size (L). σ_1 stands for matrix conductivity, σ_1 is free electrolyte conductivity in the pore space. σ_3 is the conductivity for the surface grid, which contains both free electrolyte and bound water.
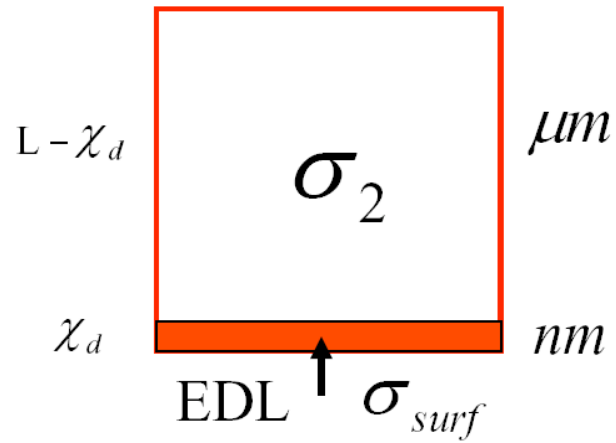
Figure 7: Conductivity model for the surface grids at grain-electrolyte interface (σ_3 in Fig 6). Gird size is L and grid conductivity is σ_3. An electric double layer (EDL) with length χ_d at nanometer scale is included in the grid with surface conductivity, σ_{surf}. The remainder of the grid ($L - \chi_d$) has conductivity of σ_2, which is the free electrolyte conductivity in the pore space.

Ionic Strength (I, M)	Debye Length $(\chi_d,\text{Å})$
10^{-6}	3000
10^{-5}	960
10^{-4}	300
10^{-3}	96
10^{-2}	30
10^{-1}	9.6

Table 5: Deby length as a function of electrolyte ionic strength (Morgan et al., 1989).
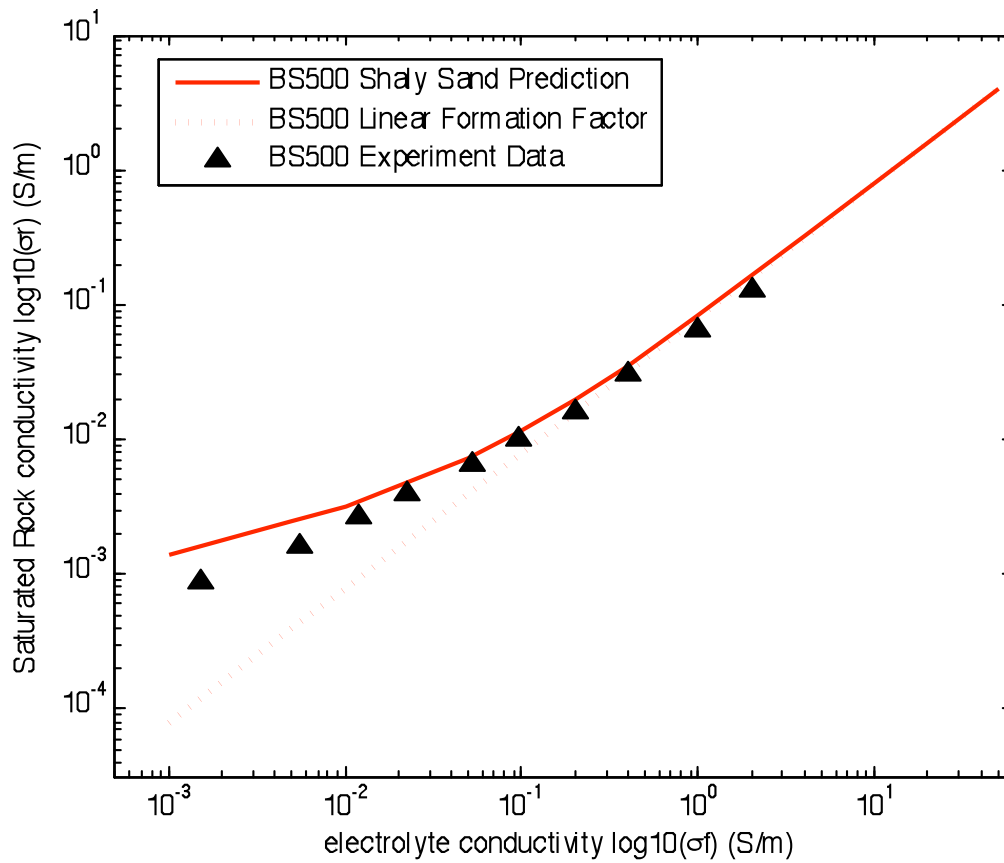
Figure 8: Linear relationship between electrolyte conductivity and saturated BS500 conductivity using two phase model (dashed line). Shaly sand behavior prediction using three–phase model (solid line). Laboratory measurements are shown as triangles.
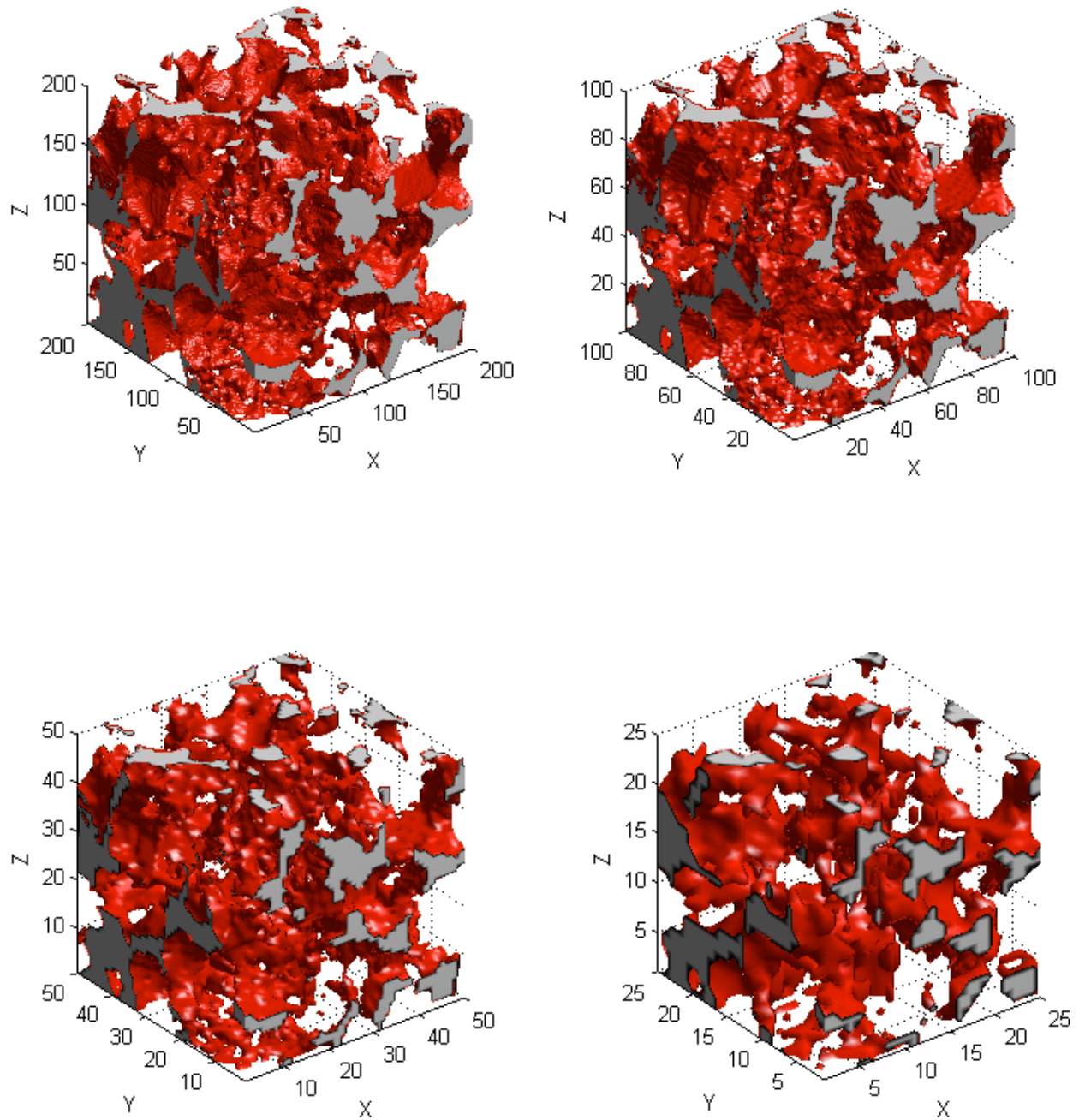
Figure 9: 3D pore structure of the downscaled cubes from original 400^3 cube (Fig 1b) using majority rule. Connectivity of the pore space and thin pore throat is getting lost with decreasing image resolution.
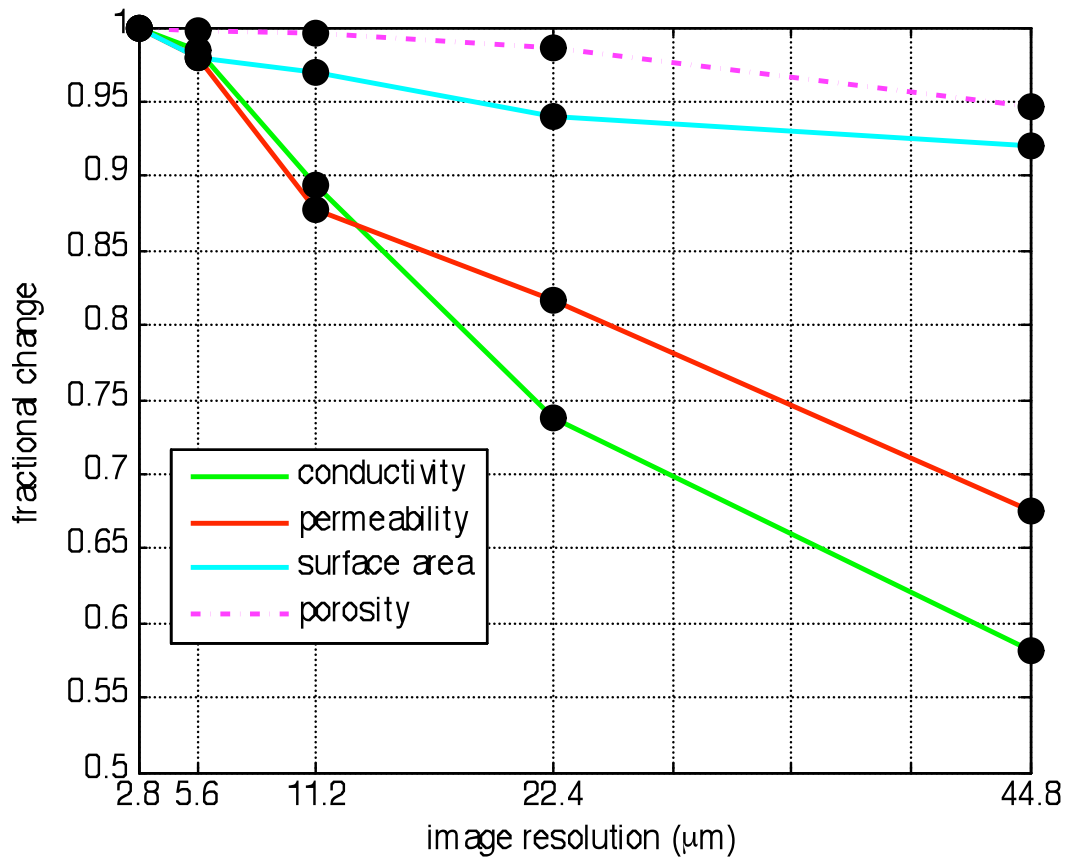
Figure 10: Fractional change in numerically computed porosity, electrical conductivity, permeability and surface area from 400^3 cube with 2.8 micron resolution to 25^3 cube with 44.8 micron resolution.